Letter Vol. 6, No. 4 / April 2019 / Optica 514

optica

High-speed van der Waals heterostructure tunneling photodiodes integrated on silicon nitride waveguides

Yun Gao, Guodong Zhou, Hon Ki Tsang, and Chester Shu*

Department of Electronic Engineering, The Chinese University of Hong Kong, Shatin, N. T., Hong Kong, China
*Corresponding author: ctshu@ee.cuhk.edu.hk

Received 19 November 2018; revised 18 March 2019; accepted 20 March 2019 (Doc. ID 352380); published 18 April 2019

Graphene photodetectors can have broadband operation and a large bandwidth, but they usually suffer from a large dark current when biased. To solve this problem, we demonstrate van der Waals heterostructure tunneling photodiodes integrated on silicon nitride waveguides. The heterostructure is made up of layers of molybdenum disulfide, graphene, boron nitride, and graphene from bottom to top. The bottom graphene is *n*-doped by molybdenum disulfide while the top graphene layer remains *p*-doped. Between the two graphene layers, multilayer boron nitride was employed as a tunneling barrier. At ~1550 nm, high on/off current ratios larger than 10^4 were measured in the dark. A responsivity of ~0.24 A/W and a bandwidth of 28 GHz (56 GHz by deconvolving response of experimental system) were also obtained. © 2019 Optical Society of America under the terms of the OSA Open Access Publishing Agreement

https://doi.org/10.1364/OPTICA.6.000514

Optical interconnects have been proposed to alleviate the thermal bottleneck of the clock frequency in conventional electrical interconnects in CMOS integrated circuits. Optical interconnections have already found applications in data centers where they are predicted to ship more than 10 million optical transceiver units per year by 2021 [1]. To realize a high-speed network on chips, at the receiver side, photodetectors must have a high responsivity, a large bandwidth, and low noise at the telecom wavelengths. One possible route toward this goal is to construct optoelectronic devices by using two-dimensional (2D) materials like graphene, molybdenum disulfide (MoS_2), and boron nitride (BN) [2]. Their atomic thickness makes them flexible and transferable onto any planar materials without suffering from the lattice mismatch issue [1,2]. To enhance the interaction with light, 2D materials have been transferred onto optical waveguides fabricated on a dielectric such as silicon or silicon nitride [1,3–10]. For graphene photodetectors integrated on silicon waveguides, the measured largest bandwidths to date include 128 GHz with 0.18-A/W responsivity [9], 65 GHz with 76-mA/W responsivity [6], 42 GHz with 0.36-A/W responsivity [5], and 41 GHz with 7-mA/W responsivity [4] at ~1550 nm. However, due to the absence of an electrical bandgap in graphene, these graphene photodetectors usually suffer from a huge dark current operating at voltage bias. The dark current gives rise to detrimental noise in communication systems.

To overcome the dark current problem, some approaches have been proposed. By using a dual-gate bilayer graphene field-effect transistor, the on/off current ratio of the device was improved to 100 at room temperature [11]. However, the dual-gate structure is not easy to build for a waveguide-integrated photodetector. The bandgap of graphene can be tuned by adding dopant atoms like boron or nitrogen [12], but the dopants would introduce additional recombination centers. The device performance will degrade accordingly. An alternative 2D-material black phosphorus, with a narrow but finite electrical bandgap, was integrated on silicon waveguides as photodetectors. It had a responsivity of 135 mA/W (11.5 nm thick) and a moderate bandwidth of ~3 GHz at 1550 nm [13]. Unfortunately, black phosphorus is unstable at ambient conditions [14]. Alternatively, tunneling photodetectors have been reported with relatively low dark currents. A graphene/Ta_2O_5/graphene tunneling photodetector was demonstrated with a high responsivity of ~1 A/W in the mid-infrared range [3]. However, its speed was limited to 1 kHz. MoS_2 and BN have been proposed as high-quality tunneling barriers [15]. BN was used as a tunneling barrier in vertical van der Waals (vdW) light-emitting diodes to enhance the quantum efficiency [16]. At a wavelength of 532 nm, a graphene/BN/MoS_2 tunneling photodiode was reported, but its dynamic response was limited to several seconds [17]. Also, none of these tunneling photodetectors have been integrated onto a dielectric waveguide. Other layered transition-metal-dichalcogenide (TMDC)-based heterostructures mainly work in the visible wavelengths due to their relatively large electrical bandgaps. Yet, datacenter interconnects require photodetectors to operate at the telecom wavelengths.

In this Letter, we report to the best of our knowledge the first vdW heterostructure tunneling photodiode integrated on a silicon nitride (Si_3N_4) waveguide. The device exhibits a high responsivity (0.24 A/W), a large bandwidth (28 GHz), and a high on/off current ratio (exceeding 10^4) at the telecom wavelengths. Previously reported high-performance graphene photodetectors are mostly integrated on silicon waveguides. Here, following

from our recent studies on high-speed graphene-on-Si_3N_4 photodetectors [7,8,10], we choose Si_3N_4 waveguide for the heterostructure tunneling photodiode. Compared to silicon, Si_3N_4 is more suitable for CMOS-compatible backend processing. Si_3N_4 can be deposited on top of existing optical interconnects to build a new interconnect layer by low-pressure chemical vapor deposition (LPCVD) or plasma-enhanced chemical vapor deposition (PECVD). However, crystalline silicon is difficult to be grown onto existing interconnects. The lower relative permittivity of Si_3N_4 also benefits for a smaller device capacitance, which also makes Si_3N_4 a better material underneath a high-speed device [7,8].

The schematic of our device is shown in Fig. 1(a). Si_3N_4 rib waveguides were fabricated on a silicon wafer grown with a 720-nm Si_3N_4 on top of a 4-μm buried oxide. A single transverse-magnetic (TM) mode was selected (for a stronger evanescent field at the upper surface of the waveguide compared to the case of a transverse-electric mode) by focusing grating couplers to couple light into and out of the waveguide. A vdW heterostructure made up of monolayer MoS_2/monolayer graphene/multilayer BN/monolayer graphene from bottom to top was stacked atop the waveguides. Figure 1(b) displays the Raman spectrum of MoS_2/graphene on a Si_3N_4 waveguide (before BN transfer). The Raman peaks of $E12g$ and A_{1g} indicate the existence of MoS_2 and that of G and 2D indicate graphene. In previous works, 20-nm and 7-nm BN were used in graphene/BN/MoS_2 heterostructures [17,18]. Here, the multilayer BN has a thickness of ∼15 nm according to atomic force microscope (AFM) measurement. The thickness was chosen to reduce the dark current while allowing a large tunneling current. Scanning electron microscope (SEM) images of a fabricated device are shown in Figs. 1(c) and 1(d). To reduce the transmission loss from the top metal contact, the top metal was designed to have a grating-like dimension with a total length of 100 μm atop a waveguide. The metal fingers have a width of 200 nm with a period of 1400 nm.

The fabrication involves three e-beam lithography (EBL) steps. The first EBL step was used to pattern the focusing gratings and straight waveguides, followed by reactive-ion etching (RIE) to transfer the pattern onto Si_3N_4. The second EBL step defined the patterns of metal contacts (GND contacts) with subsequent thermal evaporation of Cr/Au (5/40 nm) and lift off processing. Next, a piece of monolayer MoS_2 on resist was wet transferred directly onto the devices, followed by baking and resist removal. Subsequently, (bottom) monolayer graphene, multilayer BN, and (top) monolayer graphene were wet transferred onto the Si_3N_4 waveguides. The MoS_2, graphene, and BN are all commercial chemical vapor deposited (CVD) 2D materials. The third EBL defined the patterns of signal contacts at the top followed by thermal evaporation of Au (40 nm) and liftoff processing. At last, a cleaver with precise position control was used to pattern the 2D-material stack into pieces.

The vdW heterostructure forms a tunneling photodiode in the vertical direction atop the waveguide, as depicted in Fig. 1(a). In previous MoS_2 photodetectors, MoS_2 was used to absorb light in the visible wavelengths [19,20]. Different from previous cases, here, the MoS_2 is used both to passivate the interface between graphene and Si_3N_4 and to *n*-dope the bottom graphene layer. By using MoS_2 to passivate surface states between silicon and graphene, a 3 orders of magnitude improvement of device speed was demonstrated [19]. To test the *n*-doping of graphene, the Raman spectra of graphene and MoS_2 are compared before and after the two materials are in contact with each other. The results are shown in Figs. 2(a) and 2(b). Figure 2(a) shows the Raman spectra of graphene with and without covered MoS_2. A frequency downshift of its *G* peak is observed after MoS_2 transfer. An increase of the Fermi level and *n*-doping of graphene can thus be inferred [20]. As presented in Fig. 2(b), the A_{1g} peak of MoS_2 shows a frequency upshift after it is in contact with graphene. Therefore, a reduction of the Fermi level and *p*-doping of MoS_2 are derived. Combining the observations in Figs. 2(a) and 2(b), it can be concluded that the electrons move from MoS_2 to graphene. Similar observations have also been reported in Refs. [19,20]. Multilayer BN is used as a tunneling barrier between the top and the bottom graphene layers. Above BN, the top monolayer graphene is *p*-doped by the air and the top metal contact. As a result, a *p-i-n*-like tunneling photodiode is formed in the vertical direction atop the waveguide. The top and the bottom

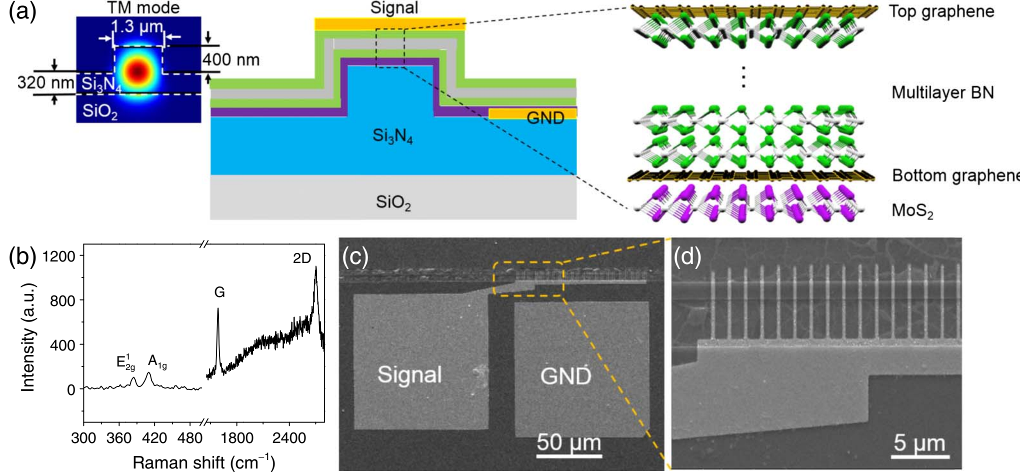

Fig. 1. Schematic of the device. (a) Schematic of a van der Waals heterostructure tunneling photodiode integrated on a Si_3N_4 waveguide. (b) Raman spectrum of a fabricated tunneling photodiode. (c) Scanning electron microscope (SEM) image of a tunneling photodiode with a length of 100 μm. (d) Magnified SEM image of the boxed region in (c) showing the metal finger electrode.

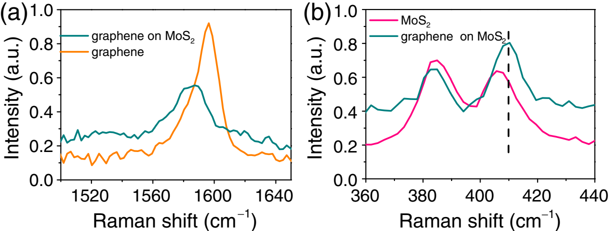

Fig. 2. (a) Raman spectra of graphene with and without in contact with MoS_2. (b) Raman spectra of MoS_2 with and without covered graphene.

graphene layers can both absorb light, but the bottom graphene layer plays a dominant role in photon absorption due to its closer distance to evanescent light along the waveguide. A strong built-in field is formed in the whole device area containing the heterojunction interface, which facilitates electron–hole separation. The hole carriers can be effectively collected by the top contact soon after they are generated.

To better understand the mechanism of carrier transport in the tunneling photodiode, we also fabricated graphene/BN/graphene and MoS_2/graphene heterostructures integrated on Si_3N_4 waveguides. Their schematics, fabrication process, and current-voltage (I-V) curves are shown in Supplement 1. The I-V curves are similar to those of previously reported graphene/BN/graphene and MoS_2/graphene heterostructures [15,20]. In a previous MoS_2/graphene photodetector, a responsivity of 0.14 A/W was measured in the near-infrared range [21]. However, the dynamic response of the device is limited to $\sim 1s$ due to the low carrier mobility in MoS_2. To achieve fast carrier transport while taking advantage of the low dark current in a tunneling device, we designed the MoS_2/graphene/BN/graphene tunneling photodiode. The carriers have a high mobility at both the top and the bottom graphene layers. When the photodiode is under forward bias (top graphene positively biased), the resulting band diagram is presented in Fig. 3(a). The electrons and holes can tunnel through the barrier efficiently. On the other hand, the band diagram of the photodiode under reverse bias (top graphene negatively biased) is shown in Fig. 3(b). Compared to the case of forward bias, fewer electrons and holes can tunnel through the BN due to a higher-energy barrier in the diode.

We first characterize the responsivity of a photodiode with a length of ~ 100 μm. The dark current of the device was measured with a bias voltage varying from −10 to +10 V, where the bottom graphene layer was grounded. The result is shown in Fig. 4(a). As expected, the current under reverse bias is smaller than that under forward bias. Benefiting from the tunnel barrier, the dark current is limited to several nA. Next, 0.42-mW light was coupled into the device to measure the photocurrent. DC probes were used to extract the current. The photocurrent is the measured current minus the corresponding dark current. As shown in Fig. 4(b), the photocurrent increases along with the forward bias while the photocurrent with reverse bias is relatively small. A breakdown was observed when the reverse bias is larger than 8 V. The above observations indicate excellent p-i-n-like photodiode characteristics. The corresponding responsivity is also shown on the right axis of Fig. 4(b). At a forward bias of 10 V, a responsivity of ~ 0.24 A/W was obtained. A maximum continuous wave (CW) optical power of ~ 200 mW was coupled into the photodetector, which functioned well without any damage. In previously demonstrated metal-graphene junction-based photodetectors [5,22], the junction region was mostly spaced several hundred nanometers away from the waveguide while most of the light was confined in the center. However, the generation and separation of electron–hole pairs happen only near the junction region. As a result, the light cannot be efficiently detected. To fully take advantage of light absorption, our photodiode is stacked directly atop the waveguide, such that the whole heterostructure area works as a junction.

Figure 4(c) plots the on/off current ratio and photocurrent-to-dark current normalized to the input optical power (NPDR) [23] as functions of the voltage bias. An on/off current ratio larger than 10^4 was derived. The current ratio shows 3 orders of magnitude improvement compared to previous graphene detectors working at the telecom wavelengths [4,5,7,9,22]. The NPDR also shows 2 orders of magnitude improvement compared to the reported result of black phosphorous detectors [13].

We next estimate the electrical bandwidth of the device by measuring its impulse response at zero bias. At a center wavelength of 1560 nm, an optical pulse train with a repetition rate of 100 MHz (Toptica FemtoFErb 1560) was coupled into the device. The full width at half-maximum (FWHM) of the pulse was measured to be ~ 1.2 ps before reaching the photodiode. A high-frequency probe (GGB Industries) was used to extract the output current, which was monitored by a 50 GHz sampling

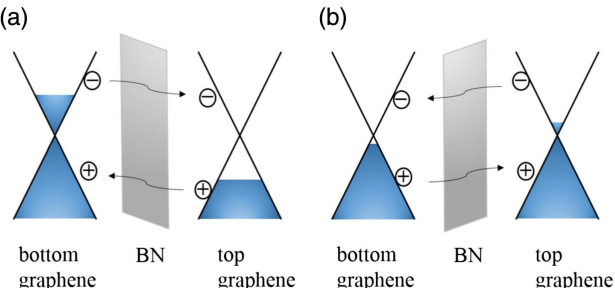

Fig. 3. Band diagram of the tunneling photodiode (a) under forward bias (top graphene positively biased) and (b) under reverse bias (top graphene negatively biased).

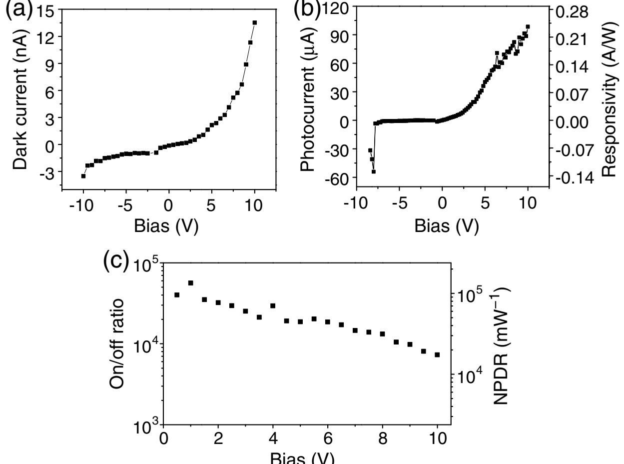

Fig. 4. Measured (a) dark current, (b) photocurrent and responsivity, and (c) on/off current ratio and NPDR of a tunneling photodetector ($L = 100$ μm) as functions of the bias voltage.

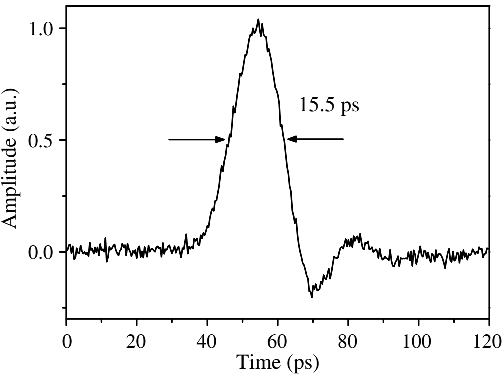

Fig. 5. Temporal response recorded by a 50 GHz sampling oscilloscope. a.u., arbitrary units.

oscilloscope (Agilent 86100A). As shown in Fig. 5, an output electrical pulse with a FWHM of ~15.5 ps was measured. We assume the pulse has a Gaussian distribution such that the relation $f_{3\,\mathrm{dB}} \times \tau_{\mathrm{tot}} = 0.441$ is satisfied, where $f_{3\,\mathrm{dB}}$ is the 3 dB frequency bandwidth and τ_{tot} is the FWHM of the electrical pulse. With the measured τ_{tot}, a bandwidth of ~28 GHz is obtained. This result includes the responses of the device and the measurement system ($\tau_{\mathrm{tot}}^2 = \tau_{\mathrm{sys}}^2 + \tau_{\mathrm{pd}}^2$). To exclude the effect of our measurement system, we tested a 65-GHz commercial photodetector by using the same equipment. After deconvolving the setup response, the bandwidth of our photodetector is derived to be ~56 GHz. This result is of 7 orders of magnitude higher than that of the graphene/Ta_2O_5/graphene tunneling photodetector reported previously [3]. The improvement is attributed to a short carrier transit time by using a narrow channel spacing and a small device capacitance. The total capacitance C_{pd} is determined by $C_{\mathrm{pd}}^{-1} = C_G^{-1} + C_Q^{-1}$, where C_G is the geometric capacitance and C_Q is the quantum capacitance [24]. C_Q is very small when the Fermi level passes through the Dirac point and so is the total capacitance [24]. The measured device bandwidth is most likely limited by the carrier transit time. A narrower channel spacing can be used to further increase the bandwidth.

To conclude, we demonstrate the first vdW heterostructure tunneling photodiode integrated on a Si_3N_4 waveguide. This device shows a relatively high responsivity (0.24 A/W), a large bandwidth (28 GHz), and a high on/off current ratio ($>10^4$) at the telecom wavelengths. This work provides a viable route toward high-bandwidth and high-sensitivity integrated photodetectors. It also paves the way for high-performance photodetectors for optical interconnects in data centers.

Funding. Research Grants Council, University Grants Committee (RGC, UGC) (14203318, 14209517); CUHK Group Research Scheme.

See Supplement 1 for supporting content.

REFERENCES

1. M. Romagnoli, V. Sorianello, M. Midrio, F. H. L. Koppens, C. Huyghebaert, D. Neumaier, P. Galli, W. Templ, A. D'Errico, and A. C. Ferrari, Nat. Rev. Mater. **3**, 392 (2018).
2. Y. Liu, N. O. Weiss, X. Duan, H.-C. Cheng, Y. Huang, and X. Duan, Nat. Rev. Mater. **1**, 16042 (2016).
3. C.-H. Liu, Y.-C. Chang, T. B. Norris, and Z. Zhong, Nat. Nanotechnol. **9**, 273 (2014).
4. D. Schall, D. Neumaier, M. Mohsin, B. Chmielak, J. Bolten, C. Porschatis, A. Prinzen, C. Matheisen, W. Kuebart, B. Junginger, W. Templ, A. L. Giesecke, and H. Kurz, ACS Photon. **1**, 781 (2014).
5. R.-J. Shiue, Y. Gao, Y. Wang, C. Peng, A. D. Robertson, D. K. Efetov, S. Assefa, F. H. L. Koppens, J. Hone, and D. Englund, Nano Lett. **15**, 7288 (2015).
6. S. Schuler, D. Schall, D. Neumaier, L. Dobusch, O. Bethge, B. Schwarz, M. Krall, and T. Mueller, Nano Lett. **16**, 7107 (2016).
7. Y. Gao, L. Tao, H. K. Tsang, and C. Shu, Appl. Phys. Lett. **112**, 211107 (2018).
8. Y. Gao, G. Zhou, N. Zhao, H. K. Tsang, and C. Shu, Opt. Lett. **43**, 1399 (2018).
9. D. Schall, E. Pallecchi, G. Ducournau, V. Avramovic, M. Otto, and D. Neumaier, "Record high bandwidth integrated graphene photodetectors for communication beyond 180 Gb/s," in *Optical Fiber Communication Conference*, San Diego, California (Optical Society of America, 2018), paper M2I.4.
10. Y. Gao, H. K. Tsang, and C. Shu, Nanoscale **10**, 21851 (2018).
11. F. Xia, D. B. Farmer, Y.-M. Lin, and P. Avouris, Nano Lett. **10**, 715 (2010).
12. P. Rani and V. K. Jindal, RSC Adv. **3**, 802 (2013).
13. N. Youngblood, C. Chen, S. J. Koester, and M. Li, Nat. Photonics **9**, 247 (2015).
14. Y. Huang, J. Qiao, K. He, S. Bliznakov, E. Sutter, X. Chen, D. Luo, F. Meng, D. Su, J. Decker, W. Ji, R. S. Ruoff, and P. Sutter, Chem. Mater. **28**, 8330 (2016).
15. L. Britnell, R. V. Gorbachev, R. Jalil, B. D. Belle, F. Schedin, A. Mishchenko, T. Georgiou, M. I. Katsnelson, L. Eaves, S. V. Morozov, N. M. R. Peres, J. Leist, A. K. Geim, K. S. Novoselov, and L. A. Ponomarenko, Science **335**, 947 (2012).
16. F. Withers, O. Del Pozo-Zamudio, A. Mishchenko, A. P. Rooney, A. Gholinia, K. Watanabe, T. Taniguchi, S. J. Haigh, A. K. Geim, A. I. Tartakovskii, and K. S. Novoselov, Nat. Mater. **14**, 301 (2015).
17. H. Jeong, H. M. Oh, S. Bang, H. J. Jeong, S.-J. An, G. H. Han, H. Kim, S. J. Yun, K. K. Kim, J. C. Park, Y. H. Lee, G. Lerondel, and M. S. Jeong, Nano Lett. **16**, 1858 (2016).
18. Q. A. Vu, J. H. Lee, V. L. Nguyen, Y. S. Shin, S. C. Lim, K. Lee, J. Heo, S. Park, K. Kim, Y. H. Lee, and W. J. Yu, Nano Lett. **17**, 453 (2017).
19. L. Tao, Z. Chen, X. Li, K. Yan, and J.-B. Xu, 2D Mater. Appl. **1**, 19 (2017).
20. W. Zhang, C.-P. Chuu, J.-K. Huang, C.-H. Chen, M.-L. Tsai, Y.-H. Chang, C.-T. Liang, Y.-Z. Chen, Y.-L. Chueh, J.-H. He, M.-Y. Chou, and L.-J. Li, Sci. Rep. **4**, 3826 (2014).
21. M. J. Park, J. K. Min, S.-G. Yi, J. H. Kim, J. Oh, and K.-H. Yoo, J. Appl. Phys. **118**, 044504 (2015).
22. X. Gan, R.-J. Shiue, Y. Gao, I. Meric, T. F. Heinz, K. Shepard, J. Hone, S. Assefa, and D. Englund, Nat. Photonics **7**, 883 (2013).
23. C. Chi On, A. K. Okyay, and K. C. Saraswat, IEEE Photon. Technol. Lett. **15**, 1585 (2003).
24. J. Gaskell, L. Eaves, K. S. Novoselov, A. Mishchenko, A. K. Geim, T. M. Fromhold, and M. T. Greenaway, Appl. Phys. Lett. **107**, 103105 (2015).